

Article

Effect of Stress Path on the Failure Envelope of Intact Crystalline Rock at Low Confining Stress

Shantanu Patel ^{1,*}  and C. Derek Martin ²

¹ Department of Mining Engineering, Indian Institute of Technology Kharagpur, Kharagpur WB 721302, India

² Department of Civil and Environmental Engineering, University of Alberta, Edmonton, AB T6G 2R3, Canada; derek.martin@ualberta.ca

* Correspondence: shantanu.patel@mining.iitkgp.ac.in

Received: 31 October 2020; Accepted: 4 December 2020; Published: 13 December 2020



Abstract: Numerical modelling is playing an increasing role in the interpretation of geological observations. A similar phenomenon is occurring with respect to the interpretation of the stress–strain response of intact rock measured in laboratory tests. In this research, the three-dimensional (3D) bonded particle model (BPM) with flat-jointed (FJ) contact was used to investigate the impact of stress paths on rock failure. The modified FJ contact model used for these studies numerically captured most of the intact rock behavior of Lac du Bonnet granite observed in the laboratory. A numerical simulation was used to track the behavior of this rock for different stress paths, starting with uniaxial tension and compression loading conditions. The migration from uniaxial tension to triaxial compression is challenging to simulate in physical laboratory tests but commonly observed around underground excavations. The numerical modelling methodology developed for this research tracks this stress path and the impact of the intermediate stress on peak strength at low confinements, commonly found around underground excavations.

Keywords: stress path; confined extension test; flat-jointed bonded particle model; intermediate principal stress

1. Introduction

Design parameters of rock typically start with the results from laboratory testing carried out for the stress conditions and the stress path expected in the field; however, as noted by Brady and Brown [1], this can rarely be achieved. Near the boundary of an underground opening, the rock can be subjected to a variety of stress conditions ranging from confined extension to confined compression [2,3]. Kaiser et al. [4] used in situ strain cells to track the stress path followed by the excavation boundary. While the rock near the boundary was initially subjected to all-around compressive stresses, by the end of the excavation those stresses had converted to confined extension. The microscale stress path followed and its damage on an intact rock during coring was investigated numerically by Bahrani et al. [5]. Developing a laboratory test methodology that can track the stress path reported by Kaiser et al. [4] is not yet possible. Consequently, the failure of rock is typically tested using simplified stress paths, such as direct tension, uniaxial compression, and triaxial compression. A consequence of this simplification is the limited ability to track the progressive fracture of rock from confined compression to confined extension.

Analyses of stress-induced failures observed around underground excavations show that the mobilized strength of sparsely fractured and massive rock masses is typically one-third to one-half the strength measured in laboratory compression tests [6–8]. The difference between the monotonic stress path used in laboratory strength tests vs. the load–unload complex stress path followed by the rock

mine-by tunnel [9] excavated in Lac du Bonnet granite and the Hoek–Brown (H–B) failure envelope obtained from laboratory triaxial testing of the rock. Point A in the σ_1 – σ_3 plot in Figure 1 represents the in situ stress condition. Path ABCDE shows the change in σ_1 and σ_3 values as construction progresses towards point A and passes through it. The dashed line near point B, $\sigma_1 - \sigma_2 = (1/3)UCS$, represents the stress level around which crack initiates in the rock. When the stress path approaches point B, microcracks start forming in the rock and, thereafter, the damage process leading to failure depends upon the stress path it takes.

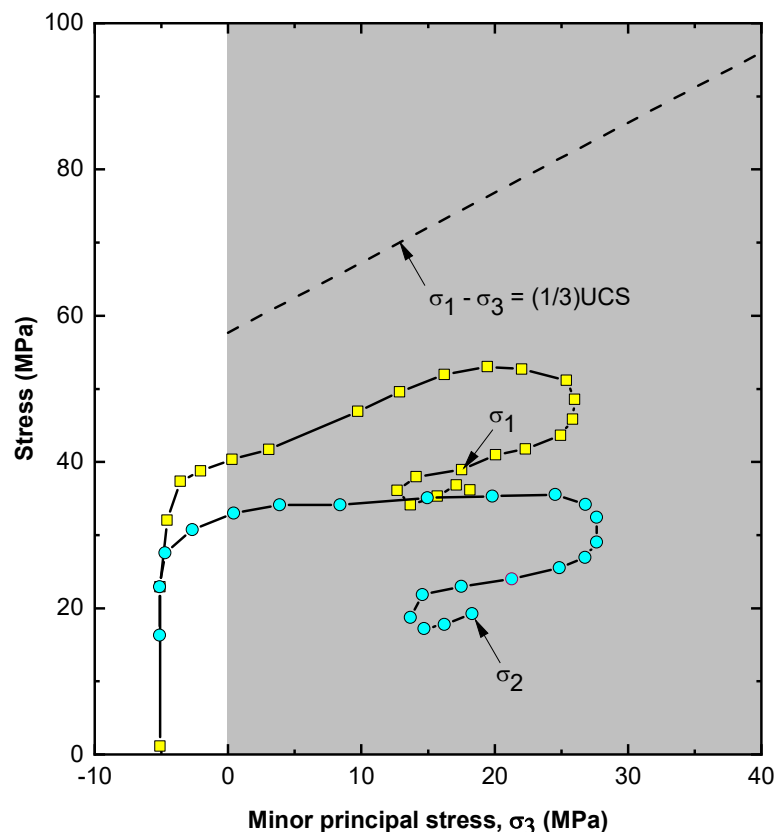


Figure 2. Stress path obtained from field measurements using CSIRO HI stress cells for σ_1 and σ_2 versus σ_3 in the hanging wall of 565#6 stope, Winston Lake Mine [4]. Note: the rock in situ stress changes from initially confined compression to confined extension.

Kaiser et al. [4] used CSIRO HI stress cells for stress measurements to obtain the stress path directly from field measurements in the hanging wall of the a mine stope. Figure 2 shows the stress path taken by σ_1 and σ_2 versus σ_3 . Comparing the initial and final stress states shows the presence of a stress rotation in addition to changes in the magnitudes of the principal stresses. Figures 1 and 2 show that, during the stress path, rock can come across a condition where one of the principal stresses can be compressive and the other tensile. This is called a confined extension condition and is explored in the next section.

2.2. Laboratory-Confined Extension Test on Rock

Confined tensile fracturing occurs in rock under mixed tensile and compressive stress conditions, and a test for this situation was proposed by Brace [19]. As shown in Figure 3, all-around compressive stress (P) and vertical compressive force (F) are initially applied to the model. The load (F) on the top and bottom platens is then gradually reduced until the specimen fractures. The confining stress in the

curved part of the sample generates the tensile stress in the central part. The compressive and tensile stresses at failure are then calculated from Equations (1) and (2):

$$\sigma_1 = \sigma_2 = P, \quad (1)$$

$$C = \sigma_3 = -\frac{P'(A_h - A_t)}{A_t} + \frac{F}{A_t}, \quad (2)$$

where C is the axial stress (positive in tension), F is the axial force (negative F acts towards sample), P is the confining pressure (positive), A_h is the head area, and A_t is the throat area. The confined extension test conducted is called the triaxial confined extension test when $\sigma_2 = \sigma_1$. Rock tested in triaxial confined extension and triaxial tests in the same range of confinement shows that samples tested in triaxial confined extension fail at a considerably higher peak stress. The data available in the literature for confined extension are very limited. Two rocks subjected to extensive triaxial confined extension tests are Carrara marble [20] and Berea sandstone [21], shown in Figure 4a,b. Patel and Martin [22] compared the biaxial strength ($\sigma_1 = \sigma_2 =$ compressive, $\sigma_3 = 0$) obtained from laboratory UCS testing of these two rocks and observed a clear impact of σ_2 on peak strength. If the confined extension test results ($\sigma_1 = \sigma_2 > \sigma_3$) are compared with triaxial test results ($\sigma_1 > \sigma_2 = \sigma_3$), there is a clear mismatch for both rock types (Figure 4). In the UCS tests, the difference is 41% and 22% for Carrara marble and Berea sandstone, respectively. The reason for this is yet unknown and could be due to the different stress path taken or the impact of σ_2 . This is explored in the next sections.

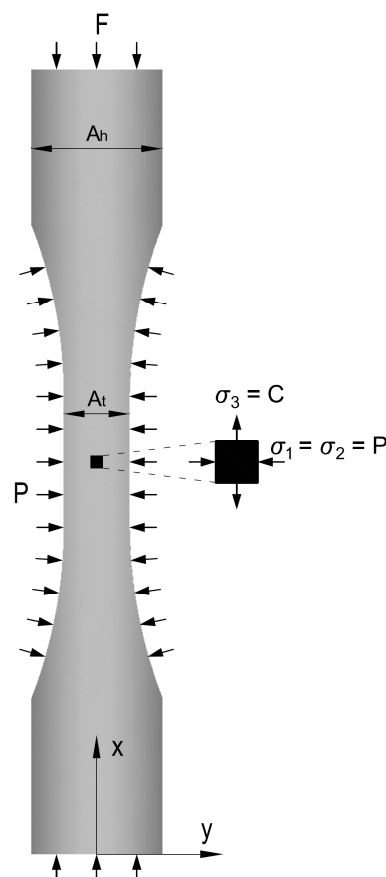


Figure 3. Confined extension test on a dog-bone-shaped rock sample (after Brace, 1964).

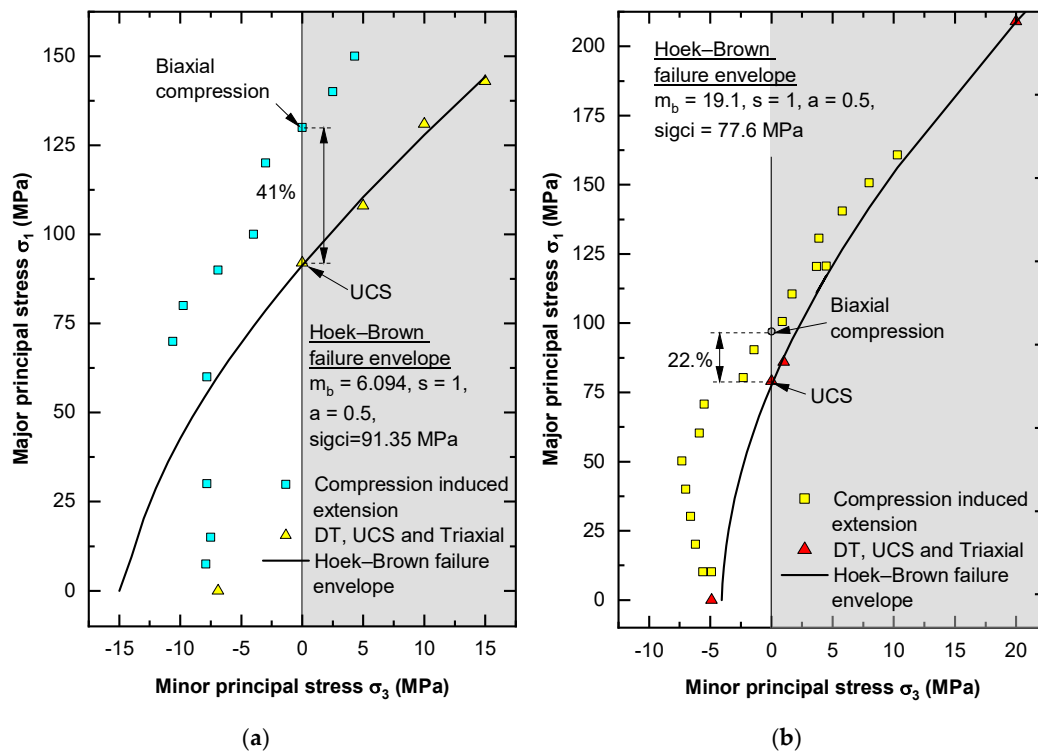


Figure 4. Results of confined extension test for (a) Carrara marble [23] and (b) Berea sandstone [21]. Direct tension (DT), UCS, triaxial compression, and confined extension test results as well as the Hoek–Brown failure envelopes are shown. The biaxial strength of the Berea sandstone was calculated using interpolation.

Patel and Martin [22] used the flattened Brazilian test to test the sample in confined extension with $\sigma_2 = 0$, where increased confinement was tested based on samples with an increased depth of flattening. However, the maximum confinement achieved using the flattened Brazilian test was 37% of the UCS. The FJ BPM was therefore used to investigate confined extension.

2.3. Flat-Jointed Bonded Particle Model

In the BPM, the mineral grains in a rock sample are represented by rigid spheres bonded at their contacts. This model has many applications from fundamental research on rock mechanics [24] to large-scale applications [25]. Potyondy and Cundall [26] first introduced the parallel BPM, which had a few shortcomings. For example, it cannot capture the high value of the UCS/ σ_t ratio of low porosity rocks [7] and requires cluster logic to increase the friction angles to more realistic values and increase the triaxial strength after calibrating the UCS [26]. Therefore, Potyondy [14] suggests the FJ BPM to address these limitations.

Figure 5a shows the 3D FJ model used in this investigation. The mineral grains are represented by grey spheres and the contacts by disk-shaped blue FJs. The FJ contacts are further discretized along the radial and tangential directions as shown in Figure 5b. Each element in the FJ contact can fail separately when an external load is applied. Potyondy [14] shows that the moment-carrying capacity of partially failed FJ is essential to produce the high UCS/ σ_t ratio. Patel and Martin [16] further investigated the role of initial microcracks present in a rock sample. They showed that an FJ sample with initial microcracks is essential to capture the initial nonlinearity, crack initiation stress, and tensile and compressive Young's moduli in addition to the UCS/ σ_t ratio of intact rock.

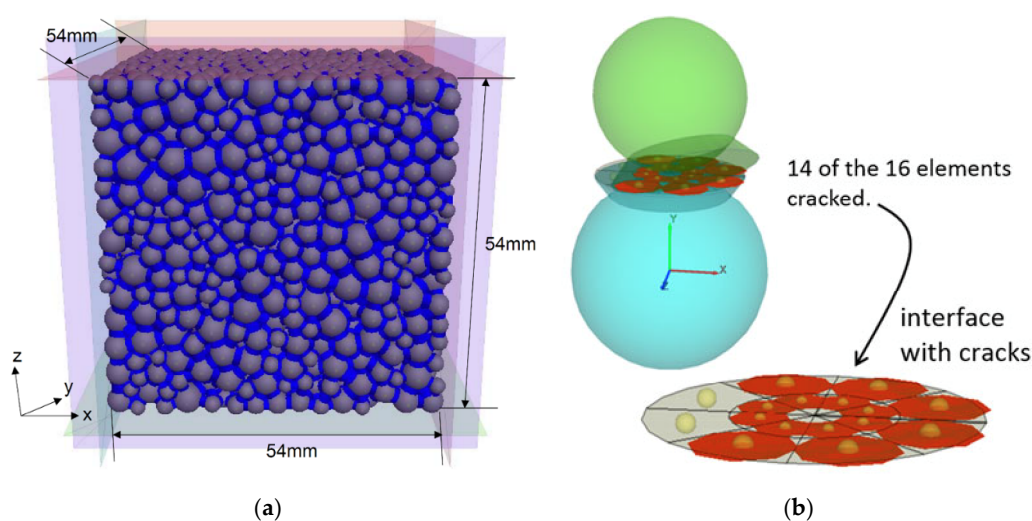


Figure 5. (a) The cubical FJ BPM made up of 3618 grains and 17,110 FJ contacts used in the investigation and (b) representation of a partially fractured FJ [24]. In the fractured FJ, 14 of the 16 elements are cracked due to bending.

3. Calibration of Microparameters for Lac du Bonnet Granite for the BPM

The first step in the FJ BPM is to obtain the microparameters for the grains and FJ contacts. These microparameters cannot be obtained experimentally and an iterative method is needed. Table 1 shows that an FJ contact requires 18 parameters for calibration, along with the parameters associated with grain-size distribution and linear material group. These parameters are described in the material modelling support manual [27]. Patel [28] describes how a set of microparameters can be efficiently obtained for a numerical rock sample to consistently reproduce the results of a real rock sample. The FJ model was used in this study to capture the rock behavior observed in the laboratory during UCS, triaxial, and direct tension tests. Using a single mineral grain type and an average of 15 particles along the width of the sample, it was possible to produce reasonable (a) bi-modularity of the rock, (b) initial nonlinearity in the axial stress–strain curve during UCS and triaxial tests, (c) crack initiation stress and crack damage stress in an UCS test, (d) ratio between the UCS and direct tension test, and (e) other responses of the laboratory sample during triaxial tests. The final set of parameters used in this investigation, which mimic the behavior of Lac du Bonnet granite, is presented in Table 1.

Table 1. List of microparameters obtained after calibration for the numerical rock sample. Parameters required for grain and material genesis are also listed [27].

Parameter	Value
<i>Associated with grain size distribution:</i>	
Minimum grain diameter	2.2 mm
Grain-size ratio	2.3
<i>Associated with material genesis:</i>	
Width of sample	54 mm
Height–width ratio	1
<i>Associated with FJ material group:</i>	
Installation gap	1.31 mm
Bonded fraction	0.65
Gapped fraction	0.35
Slit fraction, derived	0
Initial surface-gap distribution, mean	0.002 mm
Initial surface-gap distribution, standard deviation	0
Elements in radial direction	1

Table 1. Cont.

Parameter	Value
Elements in circumferential direction	3
Radius-multiplier code	0
Radius-multiplier value	0.577
Effective modulus	135.8 GPa
Stiffness ratio	1.2
Friction coefficient	1.4
Tensile-strength distribution, mean	41.6 MPa
Tensile-strength distribution, standard deviation	0
Cohesion distribution, mean	203 MPa
Cohesion distribution, standard deviation	0
Friction angle	43.2°
<i>Associated with the linear material group:</i>	
Effective modulus	135.8 GPa
Stiffness ratio	1.2
Friction coefficient	2.2 mm

3.1. Intergranular Stiffness Ratio and the Formation of Microcracks in the Sample

The ratio between the normal and shear stiffness (krat) between the mineral grains plays an important role in microcrack formation in the sample during UCS testing. Keeping the normal stiffness constant but increasing the ratio allows the intergranular slide to happen more easily, forming an early generation of crack and a higher Poisson's ratio for the numerical sample. To match the Poisson's ratio of the material, a common practice is to assume a ratio value of around 1.5 (e.g., [15]). However, we found out that, in the FJ sample during the UCS test, tensile cracks start forming at an early stage of loading (around 10% of peak) and the curve between the total number of the cracks in the numerical sample versus the axial load does not support laboratory observations. This is shown in Figure 6, where the crack generated for the numerical sample with krat = 1.6 calibrated by the laboratory macroparameters is compared with the laboratory Lac du Bonnet granite samples.

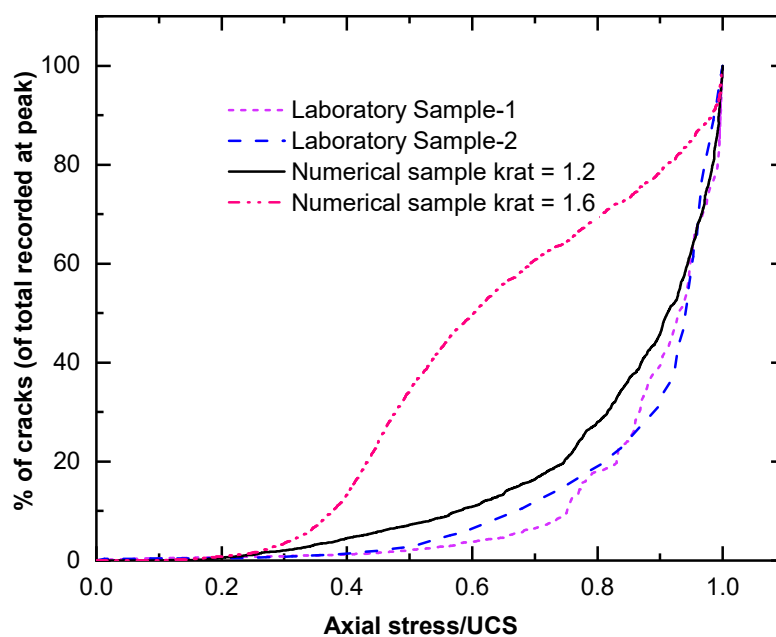


Figure 6. Comparison of microcrack formation in the numerical sample with krat = 1.6 or 1.2 and the laboratory Lac du Bonnet granite sample. The sample-1 result is from Martin [29] and the sample-2 result is from Eberhardt et al. [30]. Note the numerical samples with krat = 1.6 or 1.2 are calibrated by the same macroparameters as those for Lac du Bonnet granite.

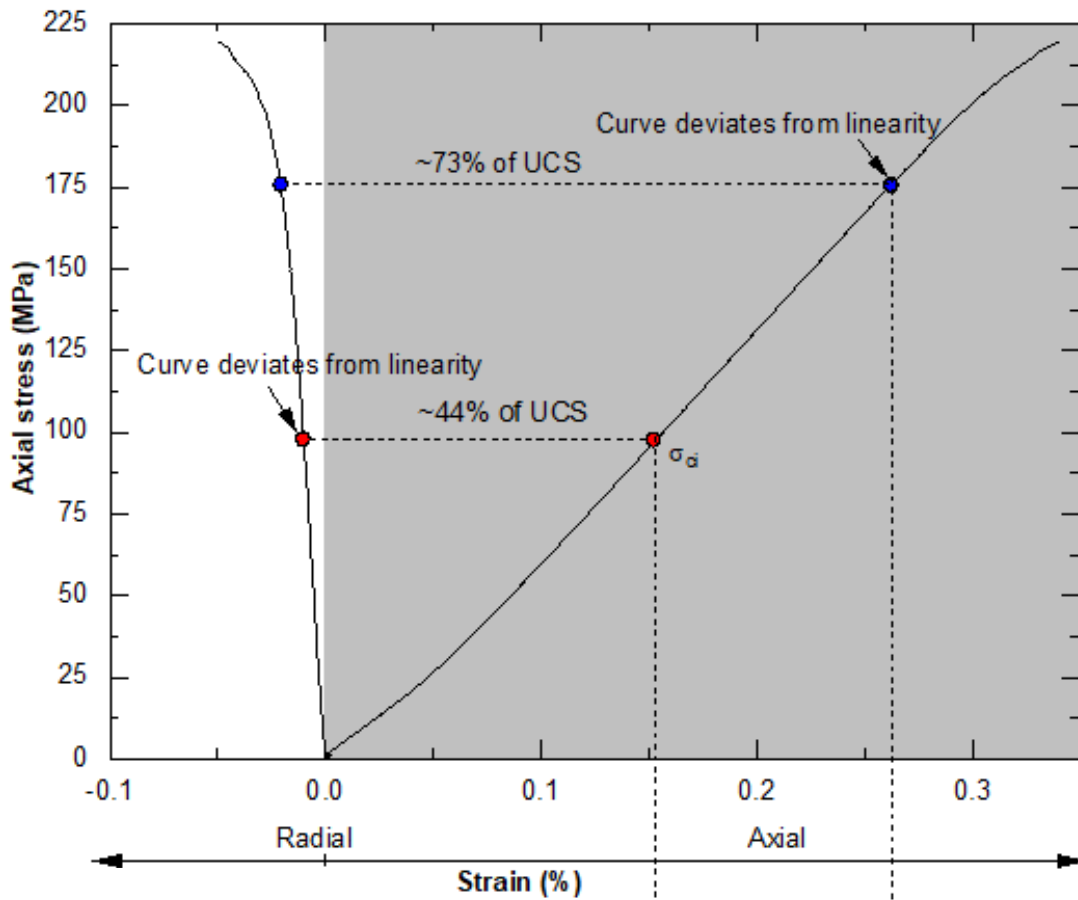
When numerical models were studied in both compression and tension, the early generation of cracks had a minor impact on the UCS test but a major impact on the confined extension tests because of the stress path. When a sample subjected to compression was tested in tension, the early microcracks considerably reduced the strength of the rock. To reduce the formation of early cracks and match the laboratory crack formation for Lac du Bonnet granite, the krat was reduced to 1.2 keeping all other microparameters constant. This changed most of the macroparameters obtained for the numerical sample. The model was then recalibrated to the direct tensile strength, Young's moduli, crack initiation stress, and peak strength from the UCS test. The corresponding set of microparameters is given in Table 1. Figure 6 shows the crack formation in the calibrated numerical sample vs. the laboratory observations. A krat of 1.2 considerably reduces the crack number and more closely matches the crack formation noted in the laboratory. Table 2 also shows that the data match most of the microparameters observed in the laboratory.

Table 2. Comparison of macroresponses observed in the laboratory Lac du Bonnet granite and numerical samples.

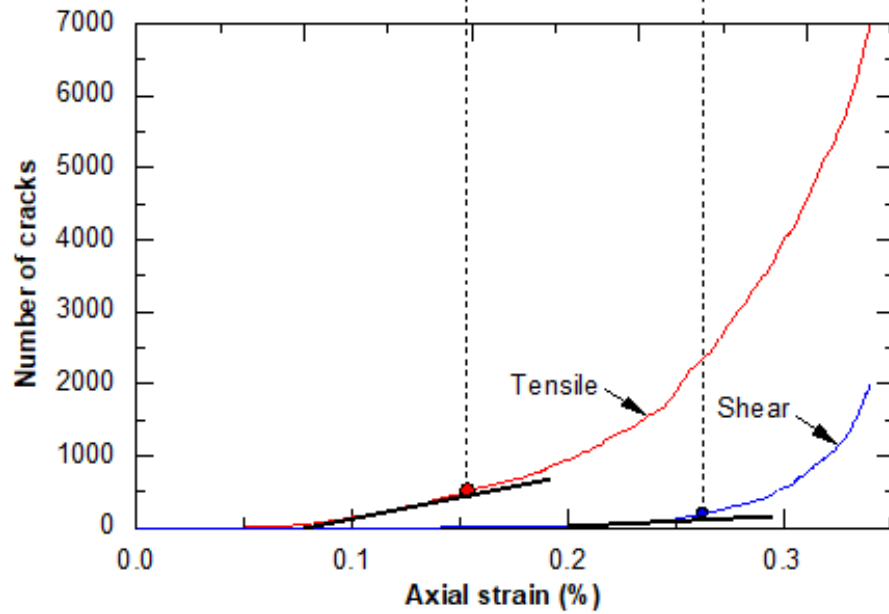
Case	E_c (GPa)	ν_c	σ_{ci} (MPa)	σ_{cd} (MPa)	UCS (MPa)	E_t (GPa)	σ_t (MPa)	E_t/E_c
Lab	70.5	0.26	88.6	163.3	221.7	45.8	10.6	0.65
Numerical	69.3	0.1	97.7	208.1	219.6	47.7	10.8	0.69

3.2. Comparison of Laboratory Response of the Lac du Bonnet Granite Sample with the FJ Numerical Sample for the UCS Test

The stress–strain curve obtained for a numerical sample with tensile and shear cracks generated due to an increase in axial strain is shown in Figure 7. The initial nonlinearity in the stress–strain curve, which is typical of UCS and triaxial rock testing, was captured by considering microgaps between the mineral grains present in the laboratory sample. The numerical sample exhibited bi-modularity (different E_t and E_c) when stress-released microfractures were included in the model. The ratio between the simulated E_t and E_c was 0.69, which is within 5% of that obtained from laboratory testing. The crack initiation stress (σ_{ci}) is the point in the axial stress vs. radial strain curve where the curve deviates from linearity after the initial elastic region; this value was 97.7 MPa for the numerical sample vs. 88.6 MPa in the laboratory. When the σ_{ci} point was projected down in Figure 7, it matched the point where tensile microcracks started forming rapidly in the sample. Because only tensile cracks formed before σ_{cd} , these cracks cannot be reflected in the axial stress versus axial strain curve. As shown in Figure 7, the axial stress versus axial strain curve deviates from linearity when the shear cracks start in the sample. These observations are in line with the laboratory findings of many researchers, such as Brace et al. [31] and Bieniawski [32]. The macroparameters for the numerical sample are compared with the Lac du Bonnet granite sample in Table 2.



(a)



(b)

Figure 7. Results of the UCS test for the numerical sample. (a) shows the axial stress versus the axial and radial strain and (b) shows the generation of tensile and shear cracks with axial strain.

4. Confined Extension Test Using the FJ BPM

As shown in Figures 1 and 2, rock around an opening may encounter confined extension conditions when σ_1 is compressive and σ_3 is tensile. Schöpfer et al. [33] and Huang and Ma [34] use the parallel BPM to investigate rock under confined extension. The present study used the FJ code to investigate the intact rock behavior in confined extensions after obtaining acceptable results for the numerical sample compared to the typical laboratory test samples.

The central part of the sample, Figure 3, used in the laboratory testing of rock in confined extension passes through the stress path ODEC, as shown in Figure 8. The sample at zero confinement (point O) is subjected to hydrostatic stress (point D). The σ_3 is then gradually reduced, keeping σ_1 and σ_2 constant until the sample fractures at point C. Samples that fail along such a stress path are influenced by σ_2 [35]. For the investigation of the confined extension on the numerical sample (Figure 3) with no σ_2 , the following steps were taken: (A) the cubical sample shown in Figure 5 was hydrostatically confined to a particular magnitude of σ_1 (point D, Figure 8); (B) keeping σ_1 constant, σ_2 and σ_3 were simultaneously reduced (point E, Figure 8); (C) the top and bottom 5 mm of the sample were then held and pulled in opposite directions keeping σ_1 constant and σ_2 at zero until the sample failed at point C (Figure 8). The x-coordinate gives the magnitude of σ_3 for the corresponding σ_1 ; and (D) steps A–C were then repeated for different magnitudes of σ_1 to obtain different failure points in confined extension.

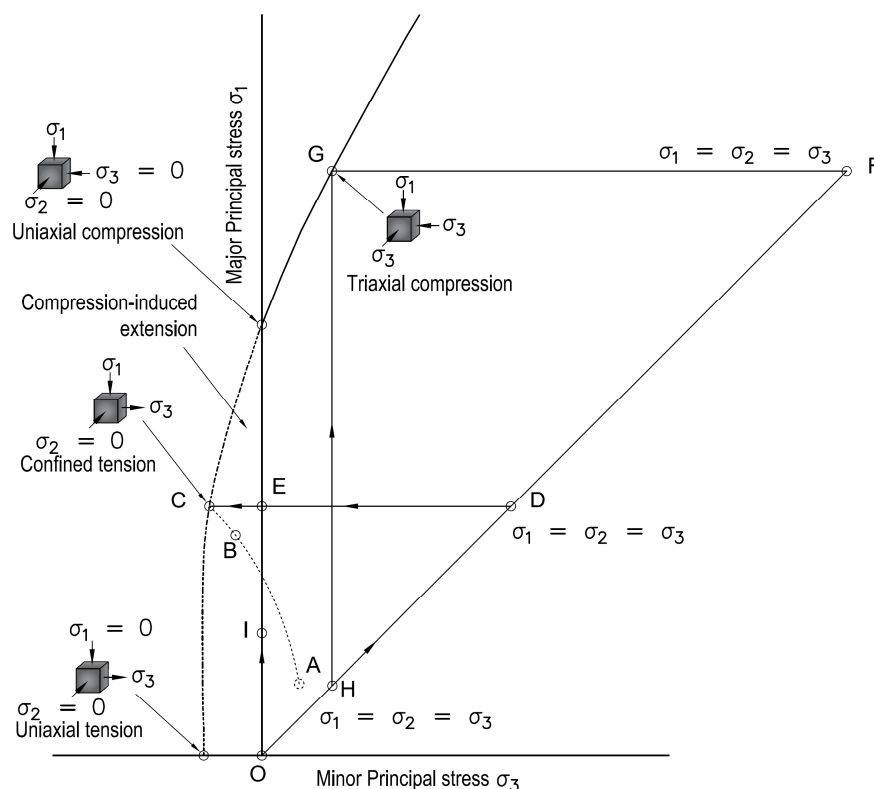


Figure 8. A typical failure envelope for rock showing the stress path during probable field-confined extension (ABC, unloading), confined extension (ODEC and OFG), and triaxial (OHG) tests. Note: the location of point A depends upon the boundary condition to which the rock is subjected in the field.

5. Results of FJ Modelling

5.1. Influence of Stress Path on a Confined Extension Test

As shown in Figure 8, point A represents an in situ stress condition with $\sigma_1 \geq \sigma_2 \geq \sigma_3$. Due to the excavation, i.e., change in the boundary condition, the rock at this point may fail in confined extension following path ABC. However, this stress path is case dependent and can be complex. The path followed by the conventional confined extension test using the dog-bone-shaped geometry is ADEC (Figure 8). The microfracture formation in rock and its peak strength are path dependent. To compare the impact of the stress path followed, paths ODEC and OEC were compared for the numerical FJ sample. As shown in Figure 9, more cracks form (533 vs. 470) in the sample when it follows stress path OEC (a low confinement stress path compared to ODEC), although the final stress conditions are similar (90 MPa at E). This influences the peak strength obtained from the samples due to the application of tensile load. As shown in Figure 10, stress paths ODEC and OEC have a 3.6% difference in peak strength.

Figure 11a,b compares the tensile and shear cracks generated in the sample when it moves from point E to point C. The number of shear cracks formed in the numerical sample is greater when the stress path followed in the laboratory is considered, which supports the results of Ramsey and Chester [20]. Stress path ODEC was considered to compare the numerical results with the laboratory results.

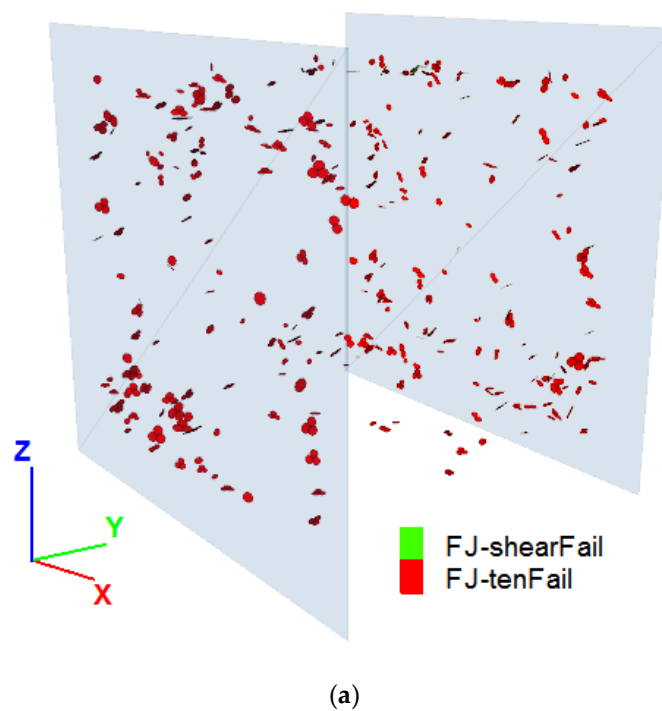


Figure 9. Cont.

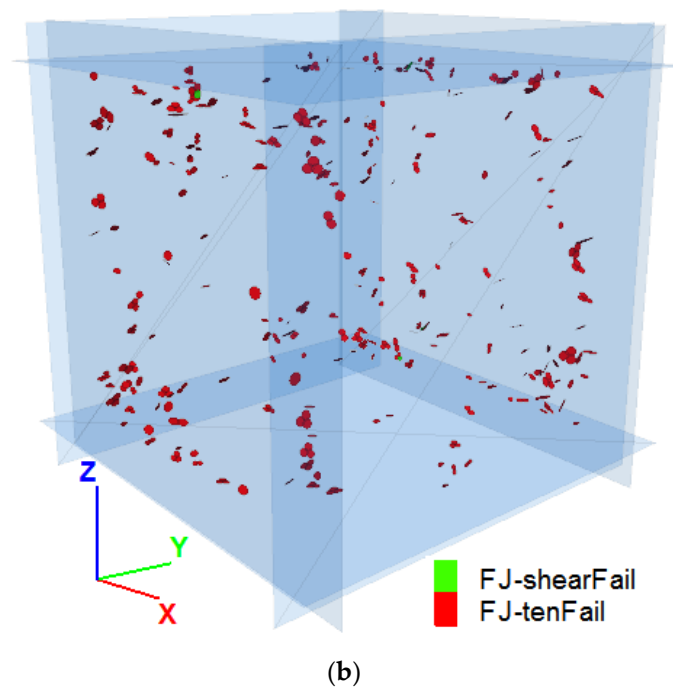


Figure 9. Cracks formed in the sample at point E when the sample follows stress path (a) OEC, $\sigma_1 = 90$ MPa, $\sigma_2 = 0$ and (b) ODEC, $\sigma_1 = \sigma_2 = 90$ MPa. (a) 533 tensile and 3 shear, (b) 470 tensile and 5 shear.

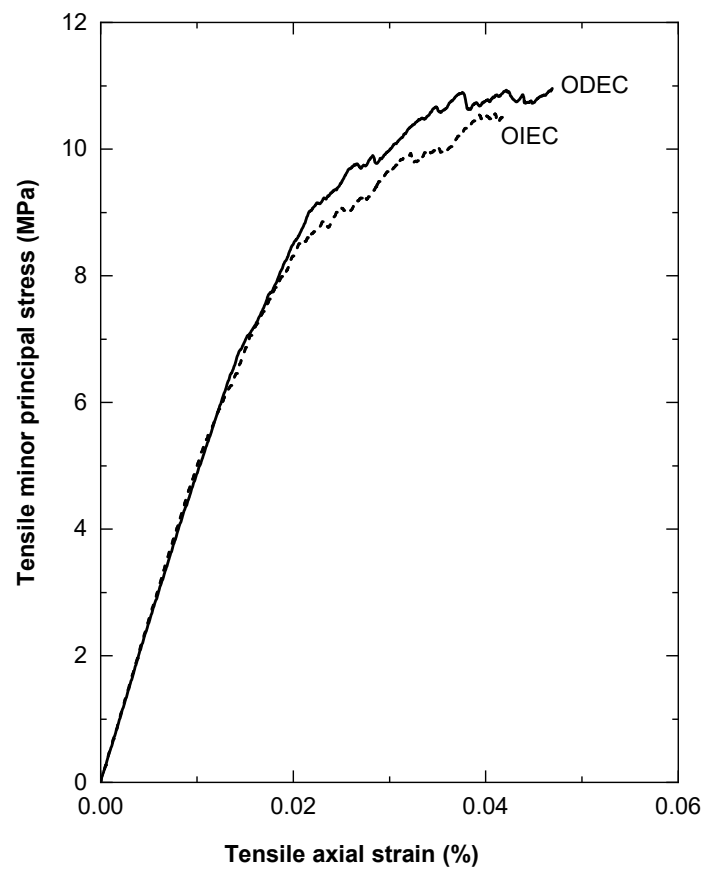
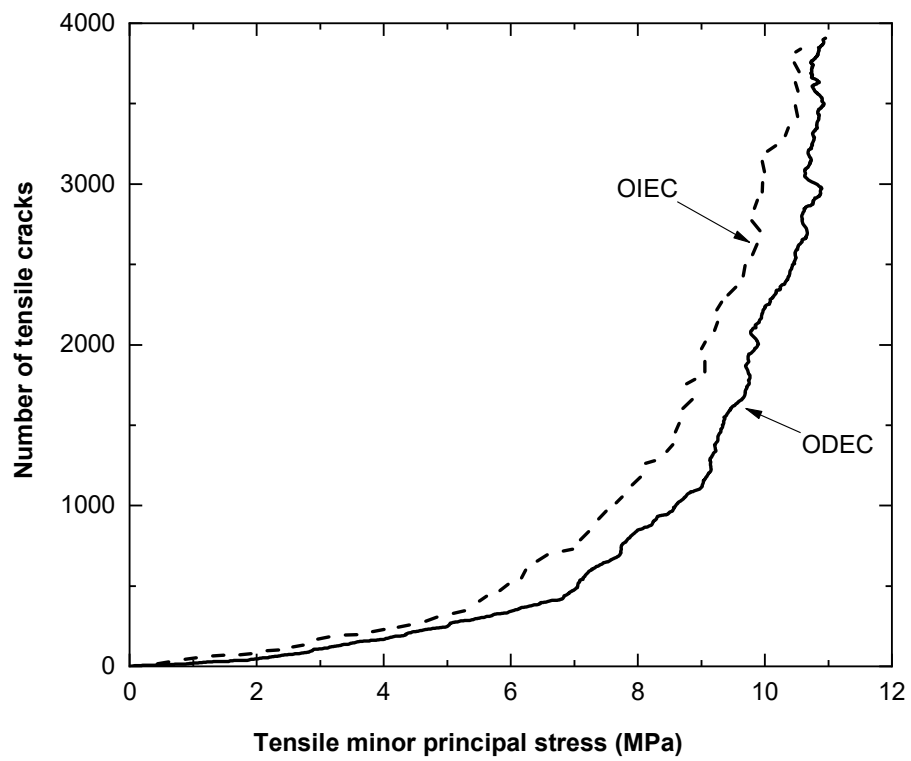
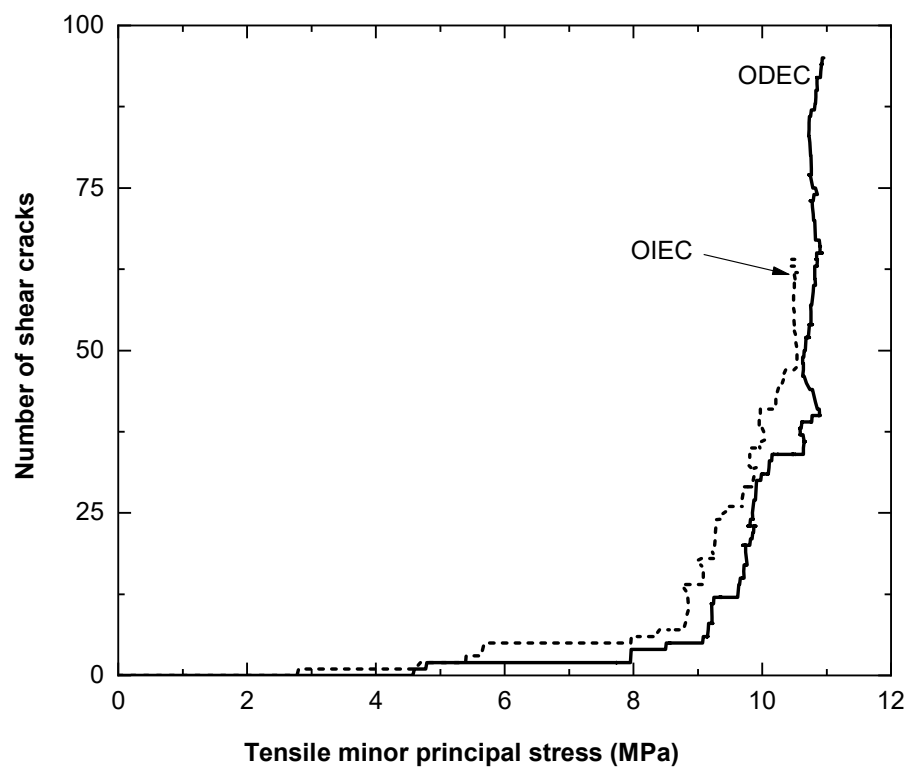


Figure 10. Tensile axial stress–strain curve obtained due to the application of tensile stress for stress paths ODEC and OEC (from point E to point C, Figure 8) at $\sigma_1 = 90$ MPa.



(a)



(b)

Figure 11. Comparison of crack development in the sample with an increase in the tensile strain from point E to point C for stress paths ODEC and OEC: (a) tensile cracks and (b) shear cracks.

5.2. Results of the Confined Extension Test with $\sigma_2 = 0$

Using the steps described in Section 4, confined extension tests were carried out at different magnitudes of σ_1 . The stress–strain results for the tests between points E and C (Figure 8) at three stress levels—low (10 MPa), medium (90 MPa), and high (150 MPa)—are shown in Figure 12. At low confinement, the sample fails similar to a direct tension test sample. However, because of the confinement, the sample fails at a higher tensile stress (i.e., similar to the Brazilian tensile strength being greater than the direct tensile strength for Lac du Bonnet granite). With an increase in confinement, the peak strength of the sample increases (up to around 50% of the UCS value). As shown in Figures 13 and 14, tensile cracking dominates at low confinement, while the percentage of shear cracks increases with increasing confinement. This finding is in agreement with observations by Brace [19] and Ramsey and Chester [20] using confined extension tests on dog-bone-shaped samples.

The confinement in the numerical sample was then increased from 10 MPa to around 80% of the UCS, which is around the σ_{cd} of Lac du Bonnet granite. When a sample with confinement more than the crack damage stress is relaxed from point D to point E (Figure 8), equilibrium is not reached and the sample fails. This observation indicates the peak strength obtained after the crack damage stress depends upon the applied boundary condition.

The sample was then further confined beyond the UCS (point F, Figure 8) and σ_2 and σ_3 gradually relaxed until the sample failed at point G (Figure 8). The results are plotted and a discussion is presented in Section 6. These results are also compared with the conventional triaxial stress (stress path OFG vs. OHG) in Section 6.

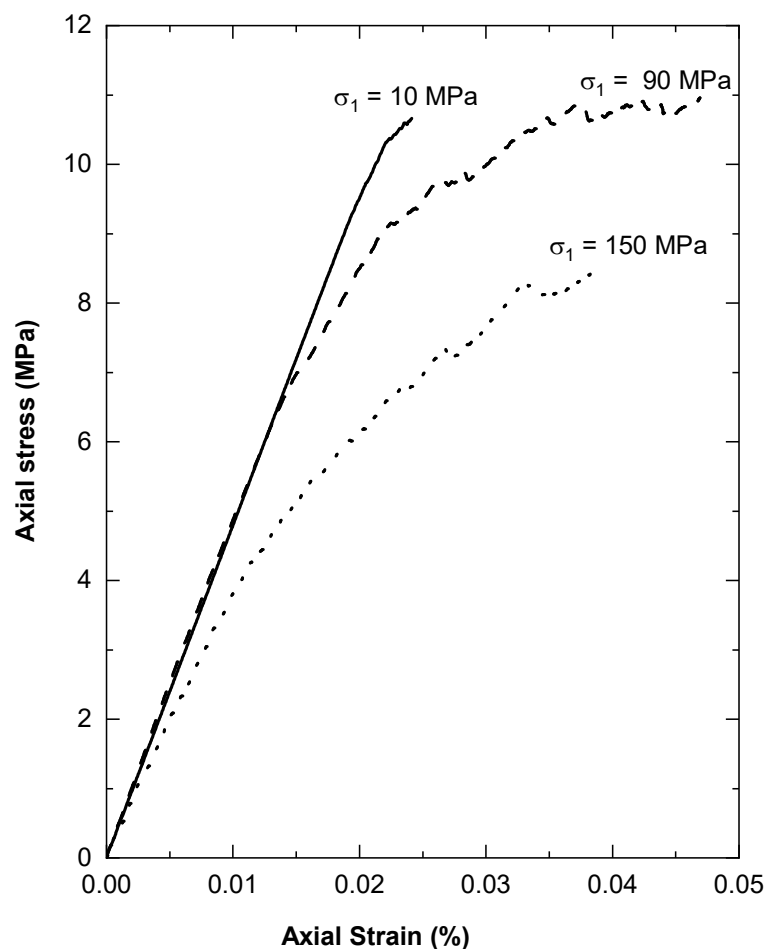


Figure 12. Stress–strain curves obtained for numerical confined extension tests at low (10 MPa), medium (90 MPa), and high (150 MPa) confinements (from point E to point C; Figure 8). In all cases, $\sigma_2 = 0$.

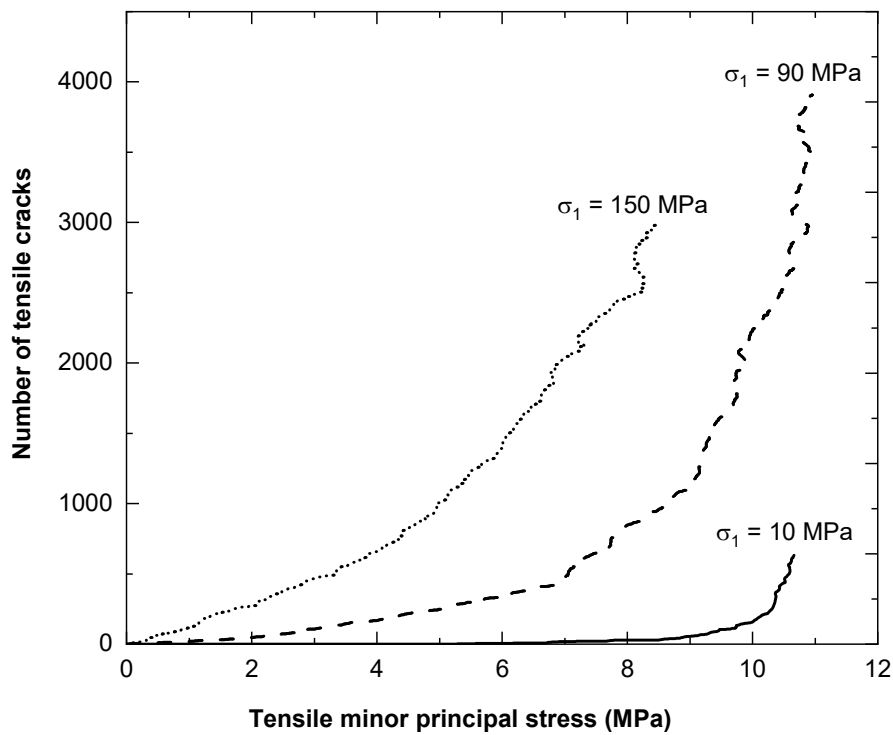


Figure 13. Number of tensile cracks formed with an increase in σ_3 for numerical confined extension tests at low (10 MPa), medium (90 MPa), and high (150 MPa) confinements (from point E to point C; Figure 8).

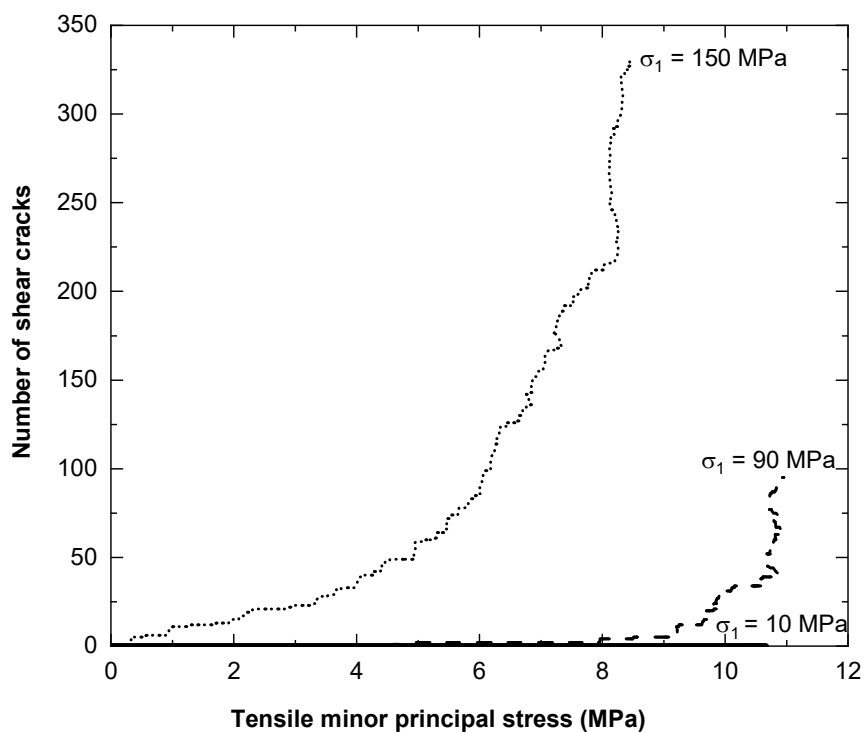


Figure 14. Number of shear cracks formed with an increase in σ_3 for numerical confined extension tests at low (10 MPa), medium (90 MPa), and high (150 MPa) confinements (from point E to point C; Figure 8).

5.3. Impact of σ_2 on the Confined Extension Test

One of the main objectives of this study was to examine the influence of σ_2 on the confined extension test of rock. A confined extension test on a numerical sample was conducted by loading the sample hydrostatically to point D (Figure 8). After point D, σ_3 was gradually reduced while keeping σ_1 and σ_2 constant. The sample was then extended in the axial direction to fail the sample in confined extension. Figure 15 compares the formation of cracks in the sample after σ_3 is unloaded (point E; Figure 8) and the sample fails in extension (point C; Figure 8) at a σ_1 of 90 MPa and three intermediate stress levels (90, 45, and 0 MPa). The cracks formed at point E (Figure 8) in the samples are random. The number of cracks formed is less when additional confinement is provided by σ_2 . σ_2 also prevents the formation of tensile cracks in the model. The shear crack percentage in the case where σ_2 is equal to σ_1 is greater than when $\sigma_2 = 0$. As shown in Figure 16, the peak strength increases from 11.0 MPa at $\sigma_2 = 0$ to 19.2 MPa when σ_2 is kept the same as σ_1 . Figure 17 compares the crack formation from points E to F (with an increase in extensile stress in the numerical sample). The number of shear cracks formed in the sample is greater when σ_2 is applied to the sample. This is in agreement with confined extension results on dog-bone-shaped Carrara marble [20].

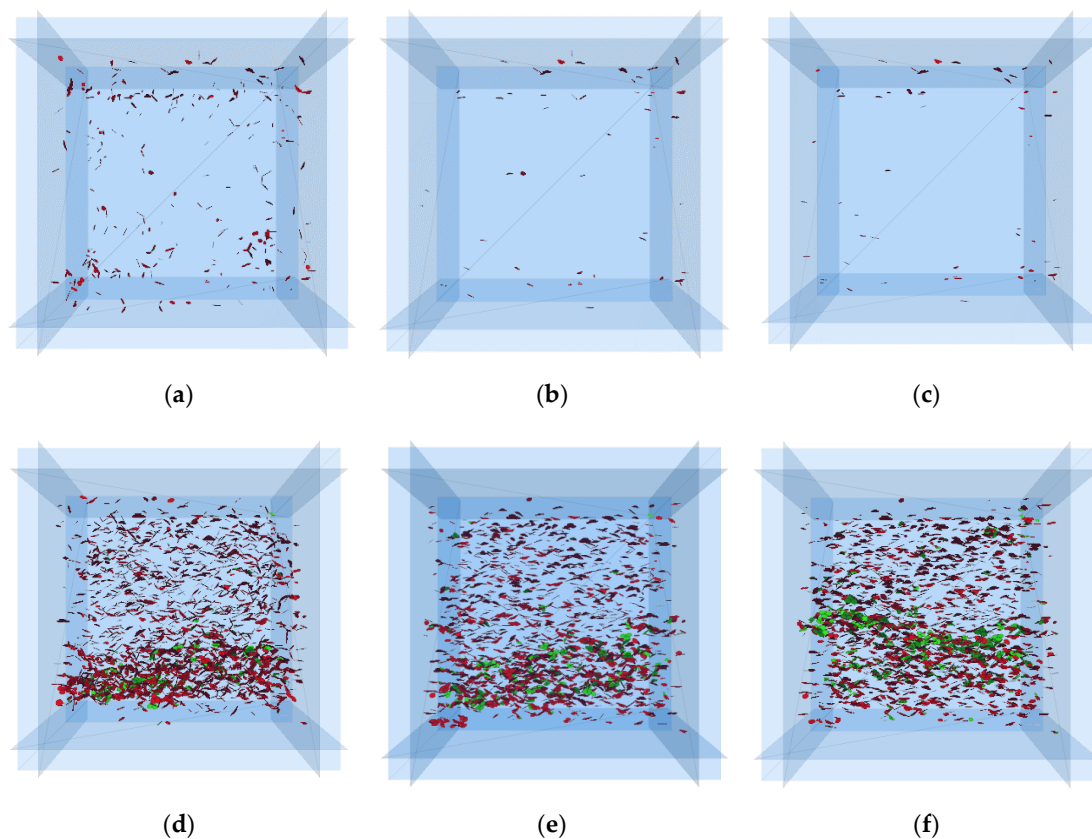


Figure 15. Comparison of crack formation in the numerical sample for stress path ODEC (Figure 8): (a–c) after the relaxation of σ_3 (point E, Figure 8) and (d–f) at peak strength (point C, Figure 8) for $\sigma_2 = 0$, $\sigma_2 = \sigma_1/2 = 45$ MPa, and $\sigma_2 = \sigma_1 = 90$ MPa. Red = tensile crack, green = shear crack. (a) $\sigma_1 = 90$ MPa; $\sigma_2 = 0$ (964 cracks); (b) $\sigma_1 = 90$ MPa; $\sigma_2 = 45$ MPa (323 cracks); (c) $\sigma_1 = \sigma_2 = 90$ MPa (204 cracks); (d) $\sigma_1 = 90$ MPa; $\sigma_2 = 0$; (e) $\sigma_1 = 90$ MPa; $\sigma_2 = 45$ MPa; (f) $\sigma_1 = \sigma_2 = 90$ MPa.

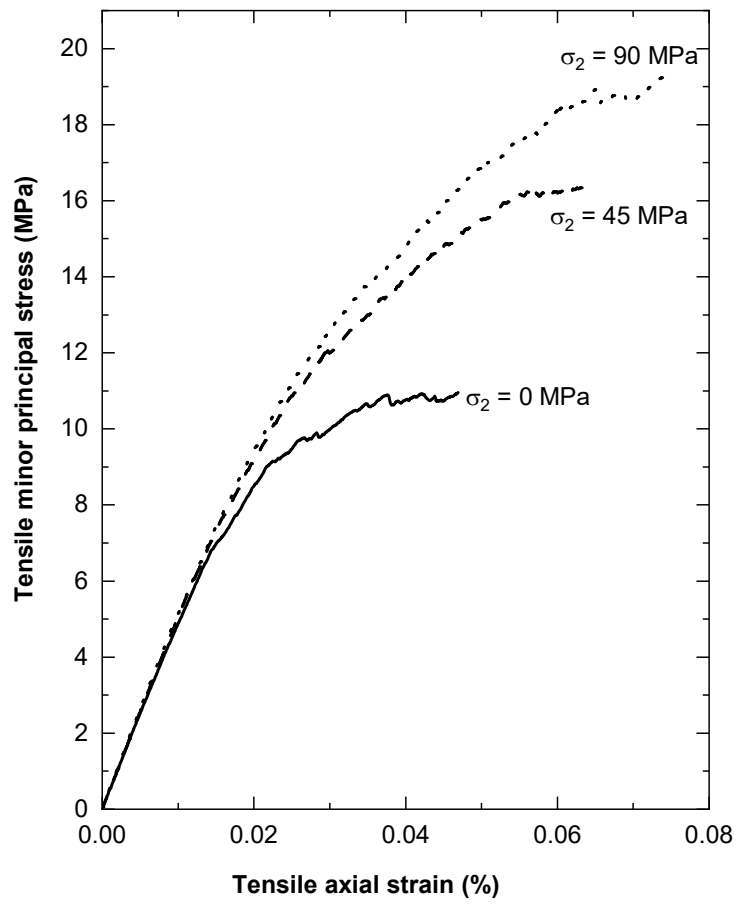
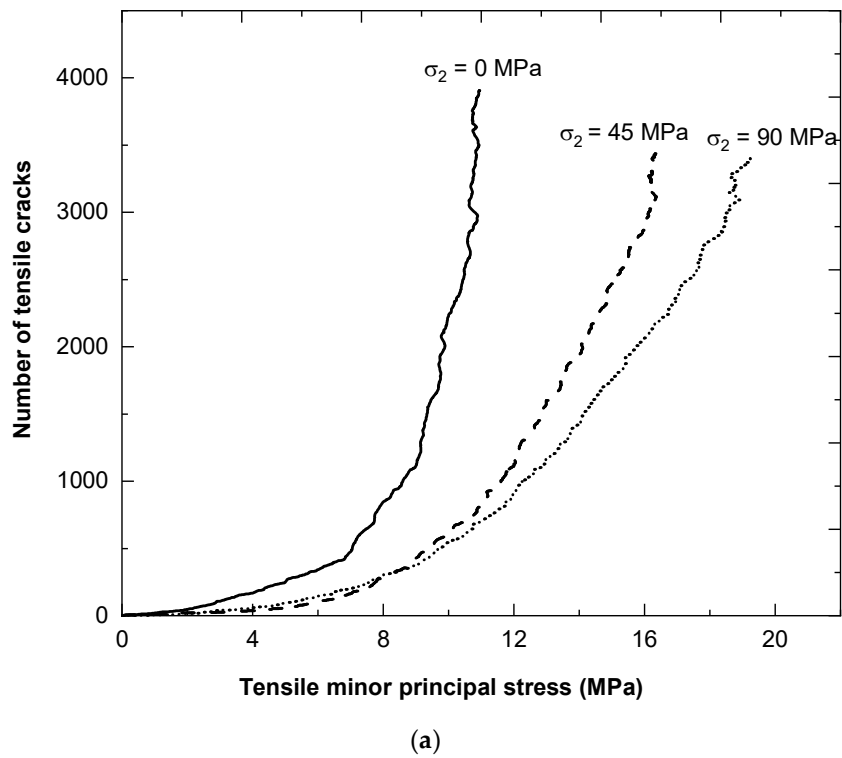


Figure 16. Confined extension test at $\sigma_2 = \sigma_1 = 90$ MPa, $\sigma_2 = \sigma_1/2 = 45$ MPa, and $\sigma_2 = 0$ (stress–strain curve showing the impact of σ_2 in the numerical sample).



(a)
Figure 17. Cont.

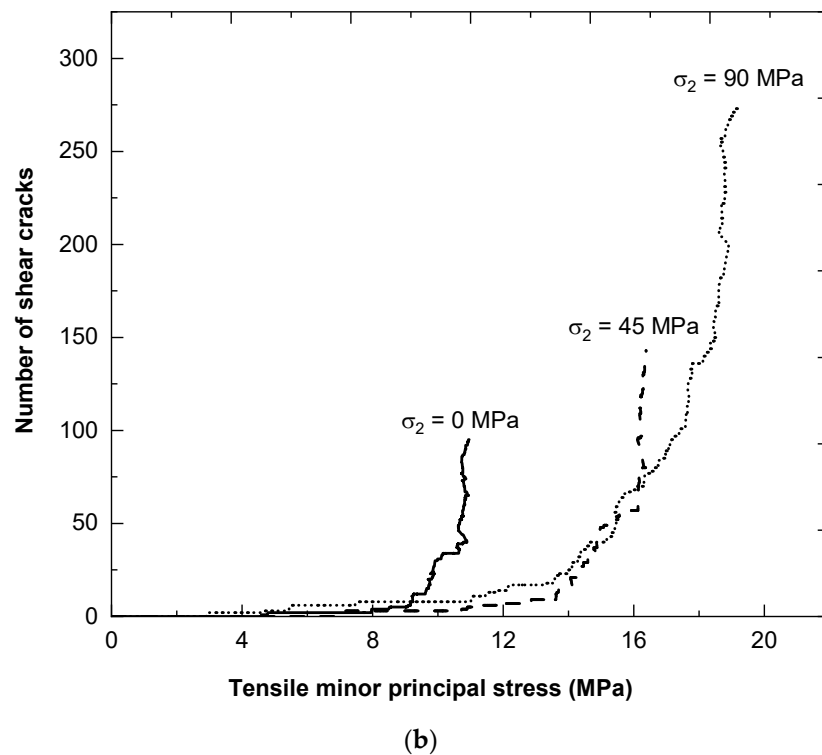


Figure 17. Comparison of crack formation in the numerical sample with an increase in σ_2 : (a) tensile cracks and (b) shear cracks. In all cases, σ_1 was kept constant at 90 MPa.

6. Failure Envelope for Lac du Bonnet Granite

The data points obtained from the direct tension (DT), Brazilian (BR), flattened Brazilian (FB), triaxial, and confined extension tests on numerical samples along with the best fit Hoek–Brown failure envelope obtained from the triaxial tests on Lac du Bonnet granite are plotted in Figure 18. The data points obtained from the confined extension test on the numerical sample pass through the laboratory testing with respect to direct tension, Brazilian and flattened Brazilian, UCS, and triaxial data. The numerical confined extension tests show a tension cutoff up to ~50% of the UCS, after which σ_3 decreases sharply with the increase in σ_1 . However, as shown in Figure 18, the confinement in the laboratory sample could not be applied beyond 80% of the UCS, which is around σ_{cd} for Lac du Bonnet granite. The numerical confined extension test was continued on the compression side (σ_1 compressive, $\sigma_3 = \sigma_2$ compressive, stress path OFG; Figure 8). Comparing these results to the conventional triaxial test on the numerical sample (stress path OAG; Figure 8) results in a good match and indicates that the influence of the stress path is negligible. When the Hoek–Brown failure envelope was extended into the confined extension region, it was found out that it underestimates actual strength compared to the laboratory direct tension, Brazilian, flattened Brazilian, and confined extension test results on numerical samples. The laboratory direct tension strength was 10.6 MPa, whereas the Hoek–Brown gave a value of 6.8 MPa.

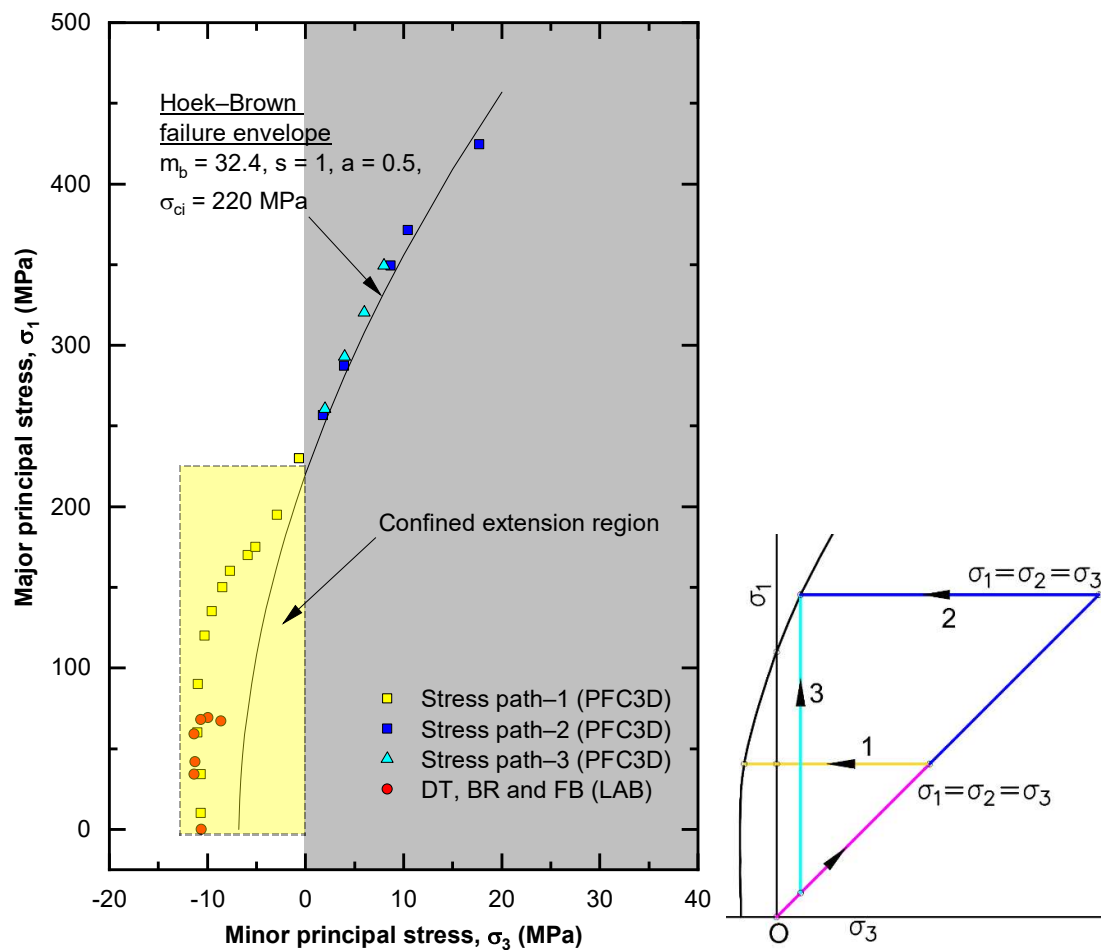


Figure 18. Results of laboratory and numerical samples on Lac du Bonnet granite. DT = direct tension, BR = Brazilian, FB = flattened Brazilian.

7. Conclusions

The FJ BPM was used in this study to capture the rock behavior observed in the laboratory during UCS, triaxial, and direct tension tests. A methodology was developed to select representative values of the microparameters for the particles and FJs in the numerical sample. With a single mineral grain type with an average of 15 particles along the width of the sample, the model could produce reasonable responses observed for Lac du Bonnet granite in the laboratory during UCS, triaxial, and direct tension tests. The code was modified to study the rock behavior in a confined extension test. The findings can be summarized as follows:

- By changing the code, it was possible to study the behavior of the rock in confined extension at $\sigma_2 = 0$. When compared with the Hoek–Brown failure criterion, the actual strength values obtained from the numerical samples in confined extension were higher than data points from the Hoek–Brown criterion; however, the Hoek–Brown failure envelope overestimated the peak strength obtained from the laboratory tests in confined extension, e.g., as in the case of Carrara marble (Figure 4a).
- The data points obtained from the Brazilian and flattened Brazilian tests were close to the values from the numerical analysis.
- Limited data available from laboratory testing (Brazilian and flattened Brazilian tests) and data from the numerical analysis indicate a tensile cutoff for Lac du Bonnet granite, as suggested by Hoek and Martin [2].

- For the numerical investigation on confined extension, the stress paths investigated have a minor impact on peak strength. However, microfracture formation was found to be path dependent.
- The numerical sample shows a clear impact of σ_2 in the confined extension test. Rock with 90 MPa confinement for both σ_1 and σ_2 produced ~76% higher strength compared to the sample with $\sigma_2 = 0$. This requires a review of the present methodology to test dog-bone-shaped specimens in confined extension.
- Further investigations should consider simultaneous stress rotation along with the stress path to better understand its impact on strength reduction in field conditions compared to the laboratory.

Author Contributions: Conceptualization, S.P. and C.D.M.; funding acquisition, C.D.M.; investigation, S.P.; supervision, C.D.M.; writing—original draft, S.P.; writing—review and editing, C.D.M. All authors have read and agreed to the published version of the manuscript.

Funding: This research was funded by the Swedish Nuclear Fuel and Waste Management Co. (SKB) Sweden, the Canadian Nuclear Waste Management Organization (NWMO), and the Natural Sciences and Engineering Research Council of Canada.

Conflicts of Interest: The authors declare no conflict of interest. The funders had no role in the design of the study; in the collection, analyses, or interpretation of data; in the writing of the manuscript, or in the decision to publish the results.

Abbreviations

σ_{ci}	Crack initiation stress
σ_{cd}	Crack damage stress
$\sigma_1, \sigma_2, \sigma_3$	Major, intermediate, and minor principal stress
DT	Direct tension test
BT	Brazilian tensile test
FB	Flattened Brazilian test
UCS	Uniaxial compressive strength

References

1. Brady, B.H.G.; Brown, E.T. *Rock Mechanics for Underground Mining*; Kluwer Academic Publishers: New York, NY, USA, 2005.
2. Hoek, E.; Martin, C.D. Fracture initiation and propagation in intact rock—A review. *J. Rock Mech. Geotech. Eng.* **2014**, *6*, 287–300. [[CrossRef](#)]
3. Hamdi, P.; Stead, D.; Elmo, D. Characterizing the influence of stress-induced microcracks on the laboratory strength and fracture development in brittle rocks using a finite-discrete element method-micro discrete fracture network FDEM- μ DFN approach. *J. Rock Mech. Geotech. Eng.* **2015**, *7*, 609–625. [[CrossRef](#)]
4. Kaiser, P.K.; Yazici, S.; Maloney, S. Mining-induced stress change and consequences of stress path on excavation stability—A case study. *Int. J. Rock Mech. Min. Sci.* **2001**, *38*, 167–180. [[CrossRef](#)]
5. Bahrani, N.; Valley, B.; Kaiser, P.K. Numerical simulation of drilling-induced core damage and its influence on mechanical properties of rocks under unconfined condition. *J. Rock Mech. Min. Sci.* **2015**, *80*, 40–50. [[CrossRef](#)]
6. Martin, C.D.; Tannant, D.D.; Kaiser, P.K. Stress path and instability around mine openings Cheminement de contraintes et instabilité d'effort autour des ouvertures de mine Spannungsweg und-instabilität um Grube Hohlräume. In Proceedings of the 9th ISRM Congress, Paris, France, 25–28 August 1999.
7. Diederichs, M.S. Instability of Hard Rockmasses, the Role of Tensile Damage and Relaxation. PhD Thesis, University of Waterloo, Waterloo, ON, Canada, 2000.
8. Andersson, J.C.; Martin, C.D.; Stille, H. The Äspö Pillar Stability Experiment: Part II-Rock mass response to coupled excavation-induced and thermal-induced stresses. *Int. J. Rock Mech. Min. Sci.* **2009**, *46*, 879–895. [[CrossRef](#)]
9. Martin, C.D. Seventeenth Canadian Geotechnical Colloquium: The effect of cohesion loss and stress path on brittle rock strength. *Can. Geotech. J.* **1997**, *34*, 698–725. [[CrossRef](#)]

10. Read, R.S.; Chandler, N.A.; Dzik, E.J. In situ strength criteria for tunnel design in highly-stressed rock masses. *J. Rock Mech. Min. Sci.* **1998**, *35*, 261–278. [[CrossRef](#)]
11. Harrison, J.P.; Hudson, J.A. Visualising and understanding the stress path for rock mechanics modelling and testing, and rock engineering design. In Proceedings of the 10th ISRM Congress, Sandton, South Africa, 8–12 September 2003; pp. 487–492.
12. Diederichs, M.S.; Kaiser, P.K.; Eberhardt, E. Damage initiation and propagation in hard rock during tunnelling and the influence of near-face stress rotation. *J. Rock Mech. Min. Sci.* **2004**, *41*, 785–812. [[CrossRef](#)]
13. Cantieni, L.; Anagnostou, G. The Effect of the Stress Path on Squeezing Behavior in Tunneling. *Rock Mech. Rock Eng.* **2009**, *42*, 289–318. [[CrossRef](#)]
14. Potyondy, D.O. A Flat-Jointed Bonded-Particle Material for Hard Rock. In *46th U.S. Rock Mechanics/Geomechanics Symposium*. Available online: <https://www.onepetro.org/conference-paper/ARMA-2012-501> (accessed on 1 January 2012).
15. Potyondy, D.O. A Flat-Jointed Bonded-Particle Model for Rock. In *52nd U.S. Rock Mechanics/Geomechanics Symposium*; American Rock Mechanics Association: Seattle, WA, USA, 2018.
16. Patel, S.; Martin, C.D. Impact of the initial crack volume on the intact behavior of a bonded particle model. *Comput. Geotech.* **2020**, *127*, 103764. [[CrossRef](#)]
17. ISRM. Suggested methods for determining tensile strength of rock materials. *Int. J. Rock Mech. Min. Sci. Geomech. Abstr.* **1978**, *15*, 99–103. Available online: <https://www.isrm.net> (accessed on 25 November 2020). [[CrossRef](#)]
18. Bieniawski, Z.T.; Bernede, M.J. Suggested methods for determining the uniaxial compressive strength and deformability of rock materials. *Int. J. Rock Mech. Min. Sci. Geomech. Abstr.* **1979**, *16*, 137–140. [[CrossRef](#)]
19. Brace, W.F. Brittle failure of rock: State of stress in the earth's crust. In *Brittle Failure of Rock: State of Stress in the Earth's Crust*; Judd, W.R., Ed.; American Elsevier: New York, NY, USA, 1964; pp. 111–180.
20. Ramsey, J.M.; Chester, M.F. Hybrid fracture and the transition from extension fracture to shear fracture. *Nature* **2004**, *428*, 63–66. [[CrossRef](#)] [[PubMed](#)]
21. Bobich, J.K. Experimental Analysis of the Extension to Shear Fracture Transition in Berea Sandstone. Master's Thesis, Texas A&M University, College Station, TX, USA, 2005.
22. Patel, S.; Martin, C.D. Application of Flattened Brazilian Test to Investigate Rocks under Confined Extension. *Rock Mech. Rock Eng.* **2018**, *51*, 3719–3736. [[CrossRef](#)]
23. Ramsey, J.M. Experimental study of the transition from brittle shear fractures to joints. Master's Thesis, Texas A&M University, College Station, TX, USA, 2003.
24. Potyondy, D.O. The bonded-particle model as a tool for rock mechanics research and application: Current trends and future directions. *Geosystem Eng.* **2015**, *18*, 1–28. [[CrossRef](#)]
25. Davoodi, A.; Asbjörnsson, G.; Hulthén, E.; Evertsson, M. Application of the Discrete Element Method to Study the Effects of Stream Characteristics on Screening Performance. *Minerals* **2019**, *9*, 788. [[CrossRef](#)]
26. Potyondy, D.O.; Cundall, P.A. A bonded-particle model for rock. *Int. J. Rock Mech. and Min. Sci.* **2004**, *41*, 1329–1364. [[CrossRef](#)]
27. Potyondy, D. Material-Modeling Support in PFC [fistPkg25]. 2017. Available online: <https://www.itascacg.com/software/pfc> (accessed on 22 November 2020).
28. Patel, S. Impact of Confined Extension on the Failure Envelope of Intact Low-Porosity Rock. Ph.D. Thesis, University of Alberta, Edmonton, AB, Canada, 2018.
29. Martin, C. The Strength of Massive Lac du Bonnet Granite around Underground Openings. Ph.D. Thesis, University of Manitoba, Winnipeg, MB, Canada, 1993.
30. Eberhardt, E.; Stead, D.; Stimpson, B. Quantifying progressive pre-peak brittle fracture damage in rock during uniaxial compression. *Int. J. Rock Mech. Min. Sci.* **1999**, *36*, 361–380. [[CrossRef](#)]
31. Brace, W.F.; Paulding, B.W.; Scholz, C. Dilatancy in the fracture of crystalline rocks. *J. Geophys. Res.* **1966**, *71*, 3939. [[CrossRef](#)]
32. Bieniawski, Z.T. Mechanism of brittle fracture of rock: Part II—Experimental studies. *Mech. Eng.* **1967**, *4*, 407–423.
33. Schöpfer, M.P.J.; Abe, S.; Childs, C.; Walsh, J.J. The impact of porosity and crack density on the elasticity, strength and friction of cohesive granular materials: Insights from DEM modelling. *Int. J. Rock Mech. Min. Sci.* **2009**, *46*, 250–261. [[CrossRef](#)]

34. Huang, H.; Ma, Y. DEM Analysis of Intact Rock Strength under Confined Tension. Available online: <http://itasca-downloads.s3.amazonaws.com/documents/Itasca%20symposia/2020/ExtendedAbstracts/02-02.pdf> (accessed on 1 January 2012).
35. Mogi, K. Effect of the intermediate principal stress on rock failure. *J. Geophys. Res.* **1967**, *72*, 5117–5131. [[CrossRef](#)]

Publisher’s Note: MDPI stays neutral with regard to jurisdictional claims in published maps and institutional affiliations.



© 2020 by the authors. Licensee MDPI, Basel, Switzerland. This article is an open access article distributed under the terms and conditions of the Creative Commons Attribution (CC BY) license (<http://creativecommons.org/licenses/by/4.0/>).